Editors' Suggestion

Pattern Formation during Melting of Lamellar Eutectics

Rahul Nellissery Rajan,[1] Rajesh Kumari Rajendran,[2] Guillaume Boussinot,[1] Kamal Sbargoud,[2] Sabine Bottin-Rousseau,[2] and Silvère Akamatsu[2]

[1]Access e.V., Intzestraße 5, 52072 Aachen, Germany

[2]Sorbonne Université, CNRS, Institut des Nanosciences de Paris, 75005 Paris, France

(Received 24 October 2025; accepted 27 May 2026; published 26 June 2026)

We present a study of the melting dynamics of a two-phase eutectic solid. *In situ*, thin-sample experiments using a transparent eutectic alloy and two-dimensional phase field simulations calibrated for the very same alloy are combined to assess pattern formation during directional melting in a temperature gradient. Depending on the melting velocity V_m and the spacing λ of the presolidified lamellar microstructure, an unexpectedly rich diversity of melting patterns is observed, with good agreement between experiments and simulations. We unravel the different physical mechanisms leading to this diversity, and establish the scaling behaviors of (i) the penetration of the liquid along the solid-solid interface at large V_m, (ii) the thickening of the primary-phase fingers at low V_m, and (iii) a period-doubling instability for small λ values. Our Letter provides a fundamental basis for further investigations of eutectic melting, including additive manufacturing during which melting or solidification cycles take place.

DOI: 10.1103/qtst-bdmt

Melting plainly refers to the reverse process of solidification. Nevertheless, the way a material melts upon heating is very different from the way crystals grow from a liquid upon cooling. Indeed, while solidification microstructures arise from self-organizing patterns at the growth front, the very same microstructures serve as an initial condition for melting. This poses deep questions of key relevance to natural phenomena [1,2] and elaboration processes [3]. Recently, this largely unexplored research topic started to attract more attention in reference to additive manufacturing, during which a material is repeatedly submitted to partial melting and solidification cycles [4,5]. In this respect, multiphase eutectics are specially attractive. Eutectic solidification delivers composite microstructures with remarkable properties [6,7], including via additive manufacturing [8–10]. It is also a paradigmatic nonequilibrium pattern formation phenomenon [11–20]. In contrast, eutectic melting has still received small attention on a fundamental level [21–24]. We propose an investigation of the melting of eutectic microstructures by combining *in situ* experiments using thin samples of a model alloy, and two-dimensional phase-field simulations calibrated for that very same alloy. The aim is to cast new light on physical mechanisms that govern steady-state melting patterns and their morphological transformations.

In a binary eutectic, two solid phases α and β coexist with the liquid at the eutectic temperature T_E. Upon cooling, the liquid solidifies into $\alpha\beta$ microstructures. Good control of their spatial distribution can be achieved in directional solidification (DS) of a nonfaceted alloy at an imposed velocity V_s in a fixed temperature gradient G. Regular (e.g., lamellar) microstructures are then delivered by periodic, coupled-growth patterns that extend in steady-state over a planar isotherm close to T_E. Depending on boundary and initial conditions, the spacing λ of a lamellar eutectic [Figs. 1(a) and 1(b)] falls close to a characteristic length, the Jackson-Hunt spacing λ_{JH}, which varies as $\lambda_{\mathrm{JH}} \sim V_s^{-1/2}$ [14,25]. The physics of the system is determined by solute diffusion in the liquid on the scale of λ, and capillary (or curvature) effects. This basic description holds for a wide range of alloy concentrations around the eutectic point, independently of G, basically owing to the overall planarity of the coupled-growth front.

For directional melting (DM), it suffices to change the sign of the sample translation speed in the temperature gradient. Yet, as illustrated in Figs. 1(c) and 1(d), eutectic melting patterns are, after an initial transient (see movies in [26]), commonly far from being planar, and a new theoretical approach has to be found.

The nonfaceted transparent CBr_4-C_2Cl_6 alloy (Table I) is a model lamellar eutectic that has been previously used for numerous solidification studies (see, e.g., Refs. [16,27]), and for eutectic melting in Ref. [21]. The chosen nominal concentration C_0 is slightly hypereutectic ($C_0 > C_E$). In the solid, the β (α) phase has a volume fraction of about 0.35 (0.65). Thin (12 μm-thick) samples are protected by flat glass walls. In the DS setup, a thermal gradient ($G = 9 \pm 1$ Kmm^{-1}) establishes by heat diffusion in the sample (axis $\mathbf{z}$) in contact with two metallic blocks regulated at temperatures T^+ and T^- ($T^+ > T_E > T^-$; see Fig. 6). Directional solidification or melting is carried out by translating the sample along $\mathbf{z}$ towards either the T^- or the T^+ block. The DS setup is placed on the XYZ stage of

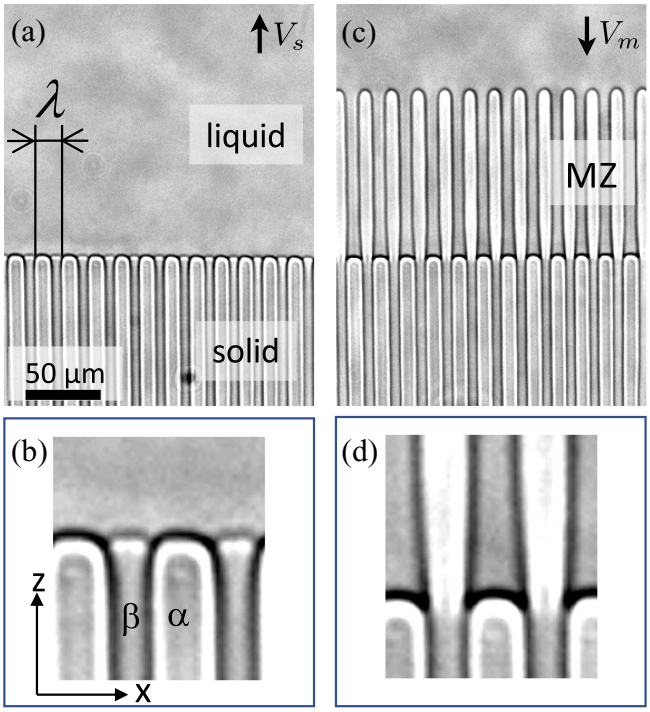

FIG. 1. *In situ* optical images in a thin CBr_4-C_2Cl_6 sample. (a) and (b) Directional solidification of a lamellar growth pattern ($V_s = 1$ µms^{-1}). (c) and (d) Directional eutectic melting pattern ($V_m = 1$ µms^{-1}) issued from the microstructure formed in (a). (b) and (d) are 4 times enlarged details of the region of the trijunctions for the patterns in (a) and (c), respectively. MZ: β-liquid coexistence region (mushy zone). α and β: eutectic solid phases. **z**: axis of the temperature gradient (**x** is parallel to the isotherms). λ: interlamellar spacing.

an optical, transmitted-light microscope equipped with a numerical camera—for more details, see Ref. [28]. For numerical simulations, we used the well-known phase-field (PF) method [18]. In the PF study of Ref. [24], the authors considered a simplified symmetric eutectic alloy. Here, we used the MICRESS software [29] for quantitative simulations implementing the physical parameters of the CBr_4-C_2Cl_6 system. We assume vanishing diffusion in the solid phases and local equilibrium at the solid-liquid interfaces. In the simulations, we set $G = 22$ Kmm^{-1} for minimizing the size of the simulation box along **z**, thus sparing computation time. We took the contact angles of the α- and β-liquid interfaces at a trijunction both equal to 60° without loosing accuracy with respect to experimental uncertainties.

TABLE I. Parameters of the CBr_4-C_2Cl_6 alloy [27]. Eutectic temperature (T_E); eutectic concentration (C_E); concentration of the eutectic solid α at T_E (C_α); concentration of the eutectic solid β at T_E (C_β); slope of the β liquidus (m_β); solute diffusion coefficient in the liquid (D); capillary length (d_0); nominal concentration of the alloy (C_0).

T_E [K]	C_E [mol%]	C_α [mol%]	C_β [mol%]	m_β [K/mol]	D [µm^2 s^{-1}]	d_0 [µm]	C_0 [mol%]
357.4	11.6	8.8	18.5	165	500	0.011	12.2

In both experiments and simulations, we first solidify a lamellar structure at V_s (1–10 µms^{-1}). The resulting spacing is close to $\lambda_{JH} = \sqrt{d_0 D/(V_s \mathcal{P})}$ [25], where d_0 is a weighted solid-liquid capillary length, D is the solute diffusion coefficient in the liquid, and $\mathcal{P} \approx 0.0293$ is an integration constant [27]. Directional melting of the solid microstructure is performed at a velocity V_m (0.1–100 µms^{-1}) close to, or much different from V_s. Figure 2 shows experimental DM patterns for various V_m values at a given λ. For comparison, PF simulations for a similar sequence are displayed in Fig. 3(a). Simulations and experiments are in a good agreement. Overall, our numerical results are also in qualitative accordance with those of Ref. [24].

The sample is fully solid below T_{TJ}, the temperature at the trijunction (TJ) [see Figs. 1(c) and 1(d)]. Above T_{TJ}, β protrudes, yielding a mushy zone (MZ) consisting of an array of apparently almost straight β fingers extending, in continuity with the β lamellae in the solid, to the tip temperature $T_{tip} > T_{TJ}$. Then, above T_{tip}, the system is fully liquid. Assuming a temperature-dependent Gibbs lever-rule condition, the hypereutectic composition C_0 provides β with the role of so-called primary phase (this role is acquired by α when C_0 lies below C_E in the hypoeutectic case), and one may at first glance understand in this way the protrusion of β. However, as shown later,

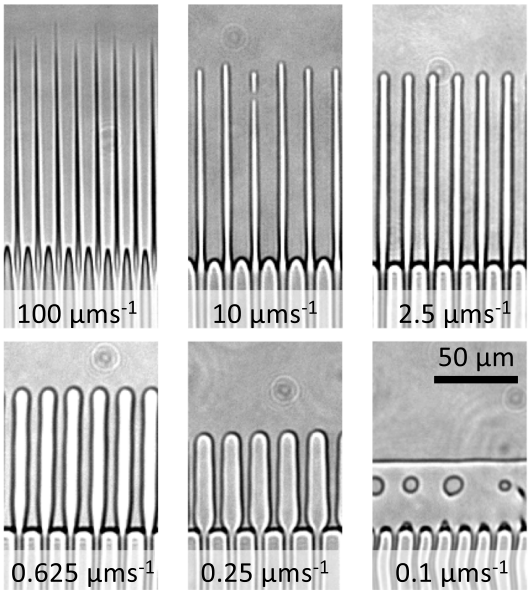

FIG. 2. *In situ* experimental snapshots (details) of directional melting patterns for various V_m. Same alloy as in Fig. 1. The thermal gradient is oriented vertically upwards. Here, the eutectic α-β structure is generated by a solidification stage at a velocity $V_s = 2$ µms^{-1}.

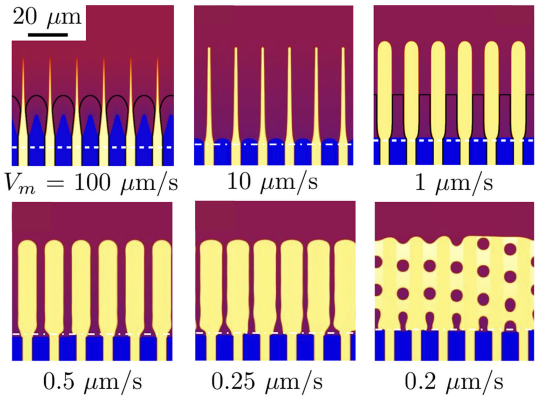

FIG. 3. Two-dimensional phase-field simulations of directional melting patterns in the CBr_4-C_2Cl_6 system at varying V_m ($V_s = 1$ μms^{-1}). The liquid is shown in red, the β phase in yellow, and the α phase in blue. The white horizontal dashed-dotted line locates the eutectic temperature, while for $V_m =$ 100 μm/s and 1 μm/s, an isoconcentration line is shown in black.

a primary solid phase melting necessarily at a higher temperature than the other solid phase should not be considered as a general rule.

Pattern formation during DM of eutectics can be described in terms of a competition between several length scales involving the four control parameters C_0, V_m, G, and λ, but also the capillary length d_0. While only two parameters, namely, V_m and λ vary in this Letter, several morphological transitions were apprehended, for example, when at low enough V_m/V_s, the actual periodicity of the eutectic melting pattern becomes a multiple of λ. Obviously, the multiplicity of characteristic length scales in competition pushes far beyond the scope of this Letter a complete unraveling of the pattern formation process during DM of eutectics. For example, since C_0 is kept constant here, the transition, when C_0 becomes close enough to C_E, from what is called "noncoupled" to "coupled" melting in Refs. [21,24] is not described here. Moreover, three-dimensional effects, imperfections of the experimental setup (for example a degradation of the sample at long melting times), or uncertainties on physical parameters, may hinder a full correspondence between the conditions of the competition between characteristic length scales in experiments and in simulations. As a consequence, qualitative differences between observed and simulated patterns may appear. For example, in contrast to the PF simulations for which we have $T_{\mathrm{tip}} \approx T_0$ where $T_0 = T_E + m_\beta(C_0 - C_E)$ is the liquidus temperature and m_β the liquidus slope, T_{tip} exceeds significantly T_0 at large V_m in experiments.

One can distinguish three different types of regions along $\mathbf{z}$ for the diffusion field in the liquid: (i) the neighborhood of the TJs where the three phases (α, β, liquid) are present, with diffusion fluxes naturally generated owing to the difference between the concentrations at the α-liquid ($C_{L\alpha}$) and the β-liquid ($C_{L\beta}$) interfaces; (ii) the MZ where the primary β crystals coexist with the liquid (the α phase is absent), and where lateral (i.e., perpendicular to the thermal gradient) and vertical (i.e., aligned with it) fluxes compete; and (iii) the bulk liquid, where vertical fluxes may develop, *a priori* on the scale of the diffusion length $l_d = D/V_m$, when T_{tip} deviates from the liquidus temperature T_0. Note that the lateral fluxes in the MZ, that increase with V_m, ensure a continuous melting of β from T_{TJ} to T_{tip}. On the other hand, the V_m-independent vertical flux in the MZ, driven by the temperature dependence of $C_{L\beta}$, ensures the melting of the β tip at the boundary between (ii) and (iii).

Up to a small curvature effect, the temperature T_{TJ} is very close to T_E. The α crystals melt close to T_{TJ}, but while the α-liquid interface is quite flat when V_m is small, it bulges significantly into the liquid when V_m is large. In the latter case (in practice, $V_m \geq 10$ μms^{-1}), the β fingers take the form of thin needles with sharp tips. Importantly, in this regime, the diffusion flux close to the TJ is perpendicular to V_m and connects the α- and β-liquid interfaces [see Fig. 8(a), blue frame]. The melting of the two solids is strongly coupled, i.e., it is driven by $\Delta C_{\mathrm{TJ}} = C_{L\alpha}(T_{\mathrm{TJ}}) - C_{L\beta}(T_{\mathrm{TJ}})$. The liquid penetration dynamics along the α-β interphase boundary is then similar, at least locally, to the one studied theoretically by Brener and collaborators [22,23]. This establishes when the length $\rho = \sqrt{d_0 D/V_m}$, which gives a measure for the radius of curvature of the interfaces close to the TJ [14,20,30,31], is much smaller than the spacing. Since $\lambda \approx \lambda_{JH}$, the condition $\rho \ll \lambda$ is equivalent to $V_m \gg V_s$. This regime is clearly reached for $V_m = 100$ μms^{-1}. Then T_{TJ} and the shape of the DM pattern in the neighborhood of the TJ are largely independent of λ and G, and the quantity ΔC_{TJ}, proportional to $T_{\mathrm{TJ}} - T_E$, scales as the Peclet number ρ/l_d. Both α- and β-liquid interfaces are slightly concave. The concentration in the liquid at the TJ lies above the two liquidus lines, outside the two-phase regions [see Fig. 8(b)], and $T_{\mathrm{TJ}} > T_E$. This yields a solute flux in the liquid from β to α, of opposite sign as compared to eutectic coupled growth. Moreover, the flux within the MZ (ii) presents a significant lateral component illustrated by the curvature of the black isoconcentration line (see Fig. 3), yielding a continuous melting of β between T_{TJ} and T_{tip}, in line with the direction of the flux near the TJ (i). Let us also note here that, for an even smaller ratio ρ/λ, nothing guarantees that α melts at a lower temperature than β, owing to the large fraction of α in the solid. This renders inoperative a hypothetical criterion stating that the solid phase melting at the highest temperature is the primary one.

When V_m decreases (here, below 10 μms^{-1}), the condition $\rho \ll \lambda$ is no longer valid. The diffusion flux close to a TJ acquires a substantial component parallel to the $\mathbf{z}$ axis [see Fig. 8(a), pink frame]. Moreover, the α-liquid interface

progressively becomes significantly convex (curvature of order $1/\lambda$), while the β-liquid interface remains slightly concave. The temperature of the TJ decreases below T_E, as previously noticed in Ref. [24], with a concentration lying inside $(\alpha + L)$ and outside $(\beta + L)$. This still permits a solute flux from β to α in the liquid, and the diffusive coupling between the two melting solids is sustained in that regime as well. In the MZ, the β fingers thicken, i.e., their width l_β increases (Figs. 2 and 3) when V_m decreases. This may be explained as follows. The lateral flux progressively vanishes as illustrated by the flatness of the black iso-concentration line at $V_m = 1$ μm/s and, when V_m is small enough, the β fingers melt only at their very tip. Then at steady state, the total amount of solute transported by diffusion in the interfinger liquid channels of width $l_L = \lambda - l_\beta$ is balanced, for conservation of mass, by the melting of the β tips at velocity V_m. Since the vertical flux in the MZ is approximately given by the quantity DG/m_β, this entails $l_L DG/m_\beta \approx l_\beta V_m(C_\beta - C_0)$, where C_β is taken at T_E (see Table I) for simplicity—we recall that in the simulations, the temperature of the tip of the β finger remains approximately equal to that of the β liquidus for C_0. Let us define the thermal length $l_t = m_\beta(C_\beta - C_0)/G$. The mass conservation can then be rewritten so as to find the β fraction $f_\beta = l_\beta/\lambda$ ($2f_\beta = l_\beta/\lambda$ for 2-λ patterns—see thereafter) in the MZ as

$$f_\beta = (1 + \mu)^{-1}, \tag{1}$$

where $\mu = l_t/l_d = V_m/V_c$. We note that the characteristic velocity $V_c = D/l_t$ is $V_c = 1.06$ μms^{-1} for the simulations, and ≈0.43 μms^{-1} for the experiments, the difference stemming from the different values of G. As shown in Fig. 4, Eq. (1) predicts well the variation of f_β in the PF simulations, evidencing the validity of the approximation for $V_m \lesssim V_c$. As expected, the PF data deviate from this law for large V_m when lateral fluxes are non-negligeable. The experimental data reported in Fig. 4 fall substantially above the numerical data. They also exhibit a large dispersion, at given V_m, which actually corresponds to a dependence of f_β on the local spacing in slightly nonuniform microstructures. More specifically, f_β decreases, and approaches the theoretical curve, when λ increases. We also shall note that uncertainties relative to image processing and/or three-dimensional effects become less important for large λ values.

While, for V_m close to V_c, eutectic melting patterns are true steady-states, we observed an oscillatory motion of the TJs about their average position when $V_m \ll V_c$. This can be interpreted as follows. For $V_m \approx V_c$, the concentration gradient in the liquid pocket $\Delta C_{TJ}/\rho$ [22] is of order G/m_β. The solute diffusion flux near the TJ essentially matches that in the MZ, which is a condition for steady-state motion at V_m. When $V_m \ll V_c$, the diffusion gradient that is

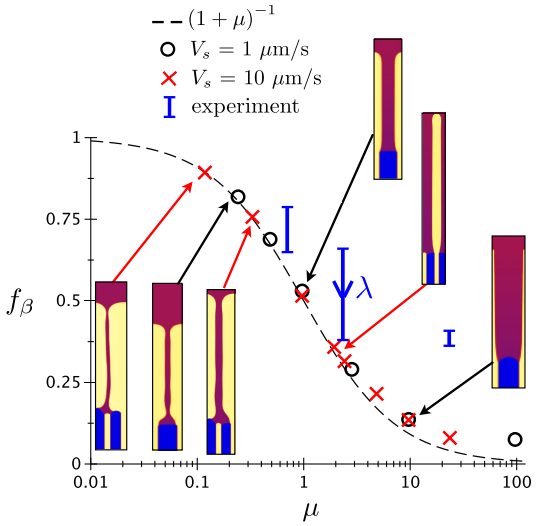

FIG. 4. Fraction of β phase f_β in the solid-liquid (MZ) region as a function of $\mu = V_m/V_c$ (see text). Symbols: PF simulations (1-λ and 2-λ patterns; see below). Blue vertical lines: experimental data (arrow: increasing λ). Dashed line: Eq. (1).

necessary for the TJ to move at V_m becomes smaller than the diffusion gradient within the MZ. This is actually accommodated by an oscillatory dynamics, with a pulsation (alternation of growth and shrinkage) of a liquid pocket in the vicinity of the TJ, and provokes an undulation of the sides of the β fingers (see Figs. 2 and 3). On average, Eq. (1) remains nevertheless valid (Fig. 4). For the lowest V_m values, the oscillatory dynamics is inefficient, and the β fingers coalesce. Melting of the primary β phase then takes place when liquid droplets, migrating owing to the so-called thermal gradient zone melting (TGZM) phenomenon [32–35] at a velocity close to V_c, reach the bulk liquid. These droplets are emitted close to the TJs; see Fig. 3. We note that the inaccurate treatment of small size droplets or liquid nucleation in PF simulations does not invalidate the qualitative picture.

Up to this point, we have mainly considered period preserving (1-λ) melting patterns. A period doubling (2-λ) instability has also been brought to light both experimentally and numerically [Figs. 5(a) and 5(c); see also Fig. 4]. We consider a lamellar microstructure with a smaller spacing than above, produced by solidification at a higher velocity ($V_s = 10$ μms^{-1}; $\lambda_{JH} \approx 4.4$ μms^{-1}). For $V_m \approx V_s$, 1-λ patterns form, in consistency with the above results. In contrast, for $V_m \ll V_s$, we observed a 2-λ instability with one β lamella out of two developing into a finger in the MZ, while the other β lamella melts close to T_E, at the same level as the α lamellae. Preliminary PF simulations demonstrate that this transition still exists in absence of thermal gradient. This deserves more investigations in the future.

Let us finally note that the observed morphological changes must go along with a rotation of the three interfaces at the TJ, as in the idealized case studied in Ref. [22].

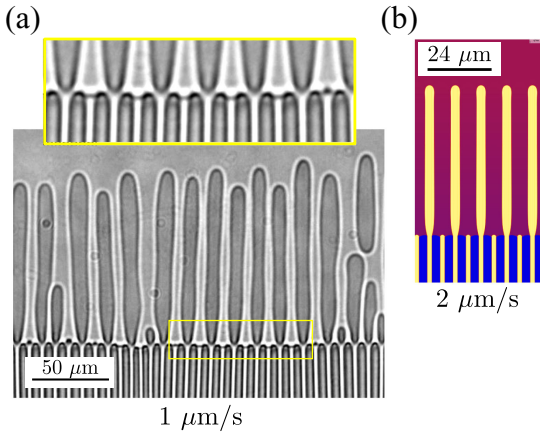

FIG. 5. (a) Experimental observation of a period-doubling ($2-\lambda$) eutectic melting pattern after V_m was decreased down to 1 μms^{-1} from $V_m = V_s = 10$ μms^{-1} (same sample as in Fig. 1). Inset: magnified view (yellow frame). (b) Phase-field simulation of a 2-λ pattern ($V_s = 10$ μms^{-1}; $V_m = 2$ μms^{-1}).

While the solid-liquid interfaces are obviously free to rotate, a bending of the α-β interphase boundaries, which are straight interfaces in the solid, also entails a local curvature that is hardly observed experimentally. In the PF simulations (also see Ref. [24]), it is enabled (and possibly exaggeratedly) by the finite diffusion across the interfaces, the diffusion coefficient varying smoothly from D in the liquid to 0 in the solid on the scale of the interface width W. However, we checked the independence of our results with respect to (reasonable) changes in W. This effect, which has been identified for a long time in PF simulations of eutectic growth (see, e.g., Ref. [18]), is still under discussion.

In conclusion, we have studied the directional melting of a regular eutectic lamellar structure, using *in situ* thin-sample experiments and two-dimensional phase field simulations in the model CBr_4-C_2Cl_6 alloy. This combined methodology allowed us to uncover the basic physical phenomena at play during the formation of different directional eutectic melting patterns, including an unprecedented morphological transition from period-preserving to period-doubling shapes. Based on the scaling behaviors of characteristic parameters, our analysis brings clear evidence that the large-scale shape of a eutectic melting pattern is essentially determined by a local diffusive coupling at the trijunction at large V_m, while it is strongly influenced by the thermal gradient when V_m decreases below a critical value. Each of these phenomena deserve further investigations. Some open questions remain to be addressed that concern, e.g., solid-state diffusion, departure from local equilibrium at interfaces, and 2D vs 3D geometries, and their effect on the eutectic melting dynamics. In view of the importance of melting in additive manufacturing, we hope that our Letter encourages new experimental and numerical studies.

Acknowledgments—We are grateful to M. Plapp and A. Karma for insightful discussions. We thank Bumedijen Raka for technical help. This work was financially supported by the collaborative, DFG and ANR project DYNAMELT (ANR-23-CE08-0035-01, DFG-530167777). We thank S. Lippmann and J. Zollinger for our fruitfull discussions within DYNAMELT.

Data availability—The data that support the findings of this article are not publicly available upon publication because it is not technically feasible and/or the cost of preparing, depositing, and hosting the data would be prohibitive within the terms of this research project. The data are available from the authors upon reasonable request.

[1] B. E. Schmidt *et al.*, Nature (London) **614**, 471 (2023).
[2] J. F. Xu, R. Shinjo, M. J. Defant, Q. Wang, and R. P. Rapp, Geology **30**, 1111 (2002).
[3] C. Zhao, B. Shi, S. Chen, D. Du, T. Sun, B. J. Simonds, K. Fezzaa, and A. Rollett, Rev. Mod. Phys. **94**, 045002 (2022).
[4] T. Keller, G. Lindwall, S. Ghosh, L. Ma, B. M. Lane, F. Zhang, U. R. Kattner, E. A. Lass, J. C. Heigel, Y. Idell, M. E. Williams, A. J. Allen, J. E. Guyer, and L. E. Levine, Acta Mater. **139**, 244 (2017).
[5] C. Körner, M. Markl, and J. A. Koepf, Metall. Mater. Trans. A **51**, 4970 (2020).
[6] C. S. Tiwary, P. Pandey, S. Sarkar, R. Das, S. Samal, K. Biswas, and K. Chattopadhyay, Prog. Mater. Sci. **123**, 100793 (2022).
[7] S. B. Kang, Adv. Mater. **36**, 2308720 (2024).
[8] A. Plotkowski, O. Rios, N. Sridharan, Z. Sims, K. Unocic, R. T. Ott, R. R. Dehoff, and S. S. Babu, Acta Mater. **126**, 507 (2017).
[9] G. Boussinot, M. Döring, S. Hemes, O. Stryzhyboroda, M. Apel, and M. Schmidt, Mater. Des. **198**, 109299 (2021).
[10] G. Boussinot, M. Döring, M. Schmidt, and M. Apel, Phys. Rev. Mater. **6**, 043405 (2022).
[11] J. S. Langer, Phys. Rev. Lett. **44**, 1023 (1980).
[12] M. Cross and P. Hohenberg, Rev. Mod. Phys. **65**, 851 (1993).
[13] G. Faivre and J. Mergy, Phys. Rev. A **45**, 7320 (1992).
[14] K. Kassner and C. Misbah, Phys. Rev. Lett. **66**, 445 (1991); Phys. Rev. A **44**, 6513 (1991); **44**, 6533 (1991).
[15] A. Karma and A. Sarkissian, Metall. Mater. Trans. A **27**, 635 (1996).
[16] M. Ginibre, S. Akamatsu, and G. Faivre, Phys. Rev. E **56**, 780 (1997).
[17] S. Akamatsu and M. Plapp, Curr. Opin. Solid State Mater. Sci. **20**, 46 (2016).
[18] R. Folch and M. Plapp, Phys. Rev. E **72**, 011602 (2005).
[19] S. Akamatsu, M. Perrut, S. Bottin-Rousseau, and G. Faivre, Phys. Rev. Lett. **104**, 056101 (2010).
[20] G. Boussinot, C. Hüter, and E. A. Brener, Phys. Rev. E **83**, 020601(R) (2011).
[21] C. A. Nordlung and R. Trivedi, Metall. Mater. Trans. A **31**, 1261 (2000).
[22] E. A. Brener and D. E. Temkin, Acta Mater. **55**, 2785 (2007).

[23] E. A. Brener, G. Boussinot, C. Hüter, M. Fleck, D. Pilipenko, R. Spatschek, and D. E. Temkin, J. Phys. Condens. Matter **21**, 464106 (2009).
[24] T. Pusztai, L. Rátkai, L. Horváth, and L. Gránásy, Acta Mater. **227**, 117678 (2022).
[25] K. A. Jackson and J. D. Hunt, Trans. Metall. Soc. AIME **236**, 1129 (1966).
[26] See Supplemental Material at http://link.aps.org/supplemental/10.1103/qtst-bdmt for a visualization of (1) Video 1—Experiment: Initial transient and steady-state directional melting of a slightly hypereutectic CBr_4-C_2Cl_6 alloy (Vm = 2 μm/s). The liquid is on top. The pulling direction is upward (parallel to the temperature gradient). The video (duration: 1580 s; accelerated 80 times) started a few seconds after the solidification (Vs = 2 μm/s) was stopped. Oscillations: imperfect temperature regulation. Horizontal dimension: 130 μm. (2) Video 2—Experiment: Steady-state directional melting of a hypereutectic CBr_4-C_2Cl_6 alloy. The video (duration: 100 s; accelerated 10 times) started 425 s after Vm was set to 4 μm/s. The lamellar eutectic microstructure was produced at Vs = 2 μm/s. Horizontal dimension: 285 μm. (3) Video 3—Phase field simulation: Initial transient and steady-state directional melting of a slightly hypereutectic CBr_4-C_2Cl_6 alloy (Vm = 1 μm/s). The liquid is at the bottom. The pulling direction is downward (parallel to the temperature gradient).
[27] J. Mergy, G. Faivre, C. Guthmann, and R. Mellet, J. Cryst. Growth **134**, 353 (1993).
[28] S. Akamatsu, K. Y. Lee, and W. Losert, J. Cryst. Growth **289**, 331 (2006).
[29] https://www.micress.de, version 7.2.
[30] G. Boussinot, C. Hüter, R. Spatschek, and E. A. Brener, Acta Mater. **75**, 212 (2014).
[31] C. Hüter, G. Boussinot, E. A. Brener, and D. E. Temkin, Phys. Rev. E **83**, 050601(R) (2011).
[32] W. G. Pfann, Trans. AIME **203**, 961 (1955).
[33] H. Nguyen-Thi, G. Reinhart, A. Buffet, T. Schenk, N. Mangelinck-Noël, H. Jung, N. Bergeon, B. Billia, J. Härtwig, and J. Baruchel, J. Cryst. Growth **310**, 2906 (2008).
[34] G. Salloum-Abou-Jaoude, G. Reinhart, H. Combeau, M. Zaloznik, T. A. Lafford, and H. Nguyen-Thi, J. Cryst. Growth **411**, 88 (2015).
[35] G. Boussinot and M. Apel, Acta Mater. **122**, 310 (2017).

End Matter

Appendix—In this End Matter section, we first provide in Fig. 6 a scheme of the experimental setup. The thin sample is in contact with two metallic temperature regulators (hot block at $T_+ > T_E$ and cold block at $T_- < T_E$) so that a thermal gradient establishes by heat diffusion across the sample. Directional solidification (melting) takes places when the sample is translated along the **z**-axis using the motor with velocity V_s (V_m) in the direction of the cold (hot) block. The *in situ* visualization is enabled by an optical, transmitted-light microscope equipped with a numerical camera (for more details, see Ref. [28]).

Second, we present in Fig. 7 the CBr_4-C_2Cl_6 phase diagram in the neighborhood of the eutectic point at C_E [27]. In addition, we locate our hypereutectic nominal composition $C_0 > C_E$.

Finally, in Figs. 8(a) and 8(b), we illustrate the features (see caption) of the two regimes, i.e., $\rho \ll \lambda$ and $\rho \sim \lambda$, with $\rho = \sqrt{Dd_0/V_m}$. In the $\rho \ll \lambda$ regime, in blue, the liquid penetrates along the α-β interface [22]. The trijunction (TJ) temperature T_{TJ} is located above T_E. In the neighborhood of the TJ, the diffusion flux is perpendicular to the growth direction, yielding here vertical isoconcentration

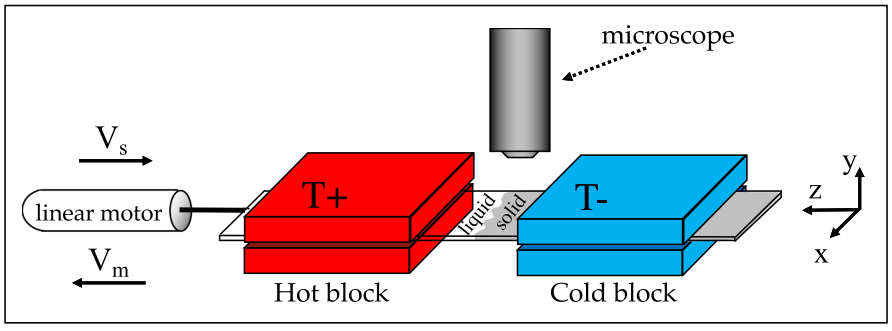

FIG. 6. Schematic representation of the thin-sample directional solidification method.

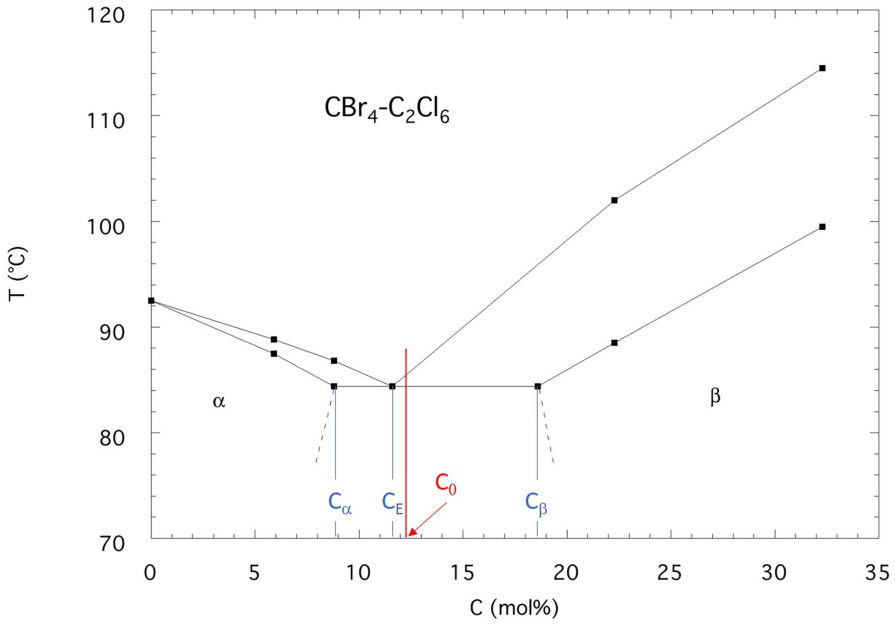

FIG. 7. Phase diagram of the CBr_4-C_2Cl_6 eutectic [27].

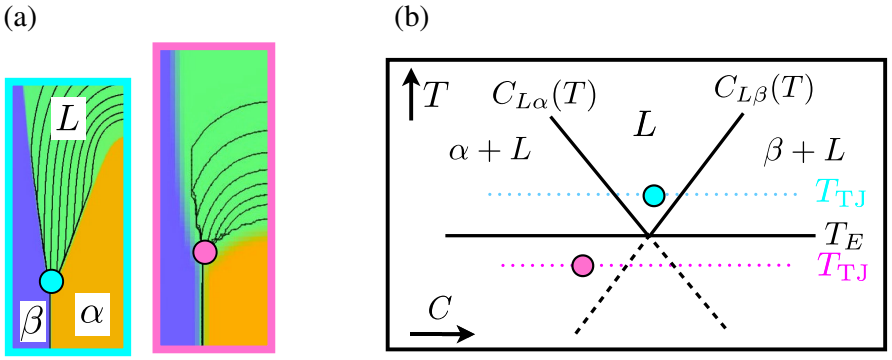

FIG. 8. (a) Focus on the trijunction (TJ) with isoconcentration lines in the liquid for the situation $\rho \ll \lambda$ (blue) and $\rho \sim \lambda$ (pink); (b) focus on the eutectic point in the phase diagram: the horizontal dotted lines schematically indicate the temperature T_{TJ} of the TJ, and the circles indicate the concentration in the liquid at the TJ.

lines. Then, at the TJ, the two solid-liquid interfaces are concave and the concentration lies outside of both two-phase regions $\alpha + L$ and $\beta + L$, each of them bounded by its liquidus line, respectively, $C_{L\alpha}(T)$ and $C_{L\beta}(T)$.

In the $\rho \sim \lambda$ regime, in pink, the diffusion flux in the neighborhood of the TJ acquires a component parallel to the growth direction, and isoconcentration lines are no more vertical. The temperature T_{TJ} is located below T_E. At the TJ, while the β-liquid interface remains concave, the α-liquid interface becomes convex. The concentration at the TJ thus lies outside the $\beta + L$ region and inside the $\alpha + L$ region.